AGU PUBLICATIONS

JGR

Journal of Geophysical Research: Atmospheres

RESEARCH ARTICLE
10.1002/2016JD026325

Key Points:
- A 1DVAR-based snowfall rate algorithm has been developed for passive microwave radiometers aboard polar-orbiting satellites
- The algorithm has been validated against both radar snowfall estimates and gauge observations with satisfactory results
- The snowfall rate product is being produced by the National Oceanic and Atmospheric Administration operationally at near real time

Correspondence to:
H. Meng,
huan.meng@noaa.gov

Citation:
Meng, H., J. Dong, R. Ferraro, B. Yan, L. Zhao, C. Kongoli, N.-Y. Wang, and B. Zavodsky (2017), A 1DVAR-based snowfall rate retrieval algorithm for passive microwave radiometers, *J. Geophys. Res. Atmos.*, *122*, 6520–6540, doi:10.1002/2016JD026325.

Received 2 DEC 2016
Accepted 23 MAY 2017
Accepted article online 1 JUN 2017
Published online 29 JUN 2017

A 1DVAR-based snowfall rate retrieval algorithm for passive microwave radiometers

Huan Meng[1], Jun Dong[2], Ralph Ferraro[1], Banghua Yan[1], Limin Zhao[1], Cezar Kongoli[2], Nai-Yu Wang[2], and Bradley Zavodsky[3]

[1]National Oceanic and Atmospheric Administration/National Environmental Satellite, Data, and Information Service, College Park, Maryland, USA, [2]University of Maryland/Earth System Science Interdisciplinary Center/Cooperative Institute for Climate and Satellites-Maryland, College Park, Maryland, USA, [3]NASA Marshall Space Flight Center/Earth Science Office Short-term Prediction Research and Transition Center, Huntsville, Alabama, USA

Abstract Snowfall rate retrieval from spaceborne passive microwave (PMW) radiometers has gained momentum in recent years. PMW can be so utilized because of its ability to sense in-cloud precipitation. A physically based, overland snowfall rate (SFR) algorithm has been developed using measurements from the Advanced Microwave Sounding Unit-A/Microwave Humidity Sounder sensor pair and the Advanced Technology Microwave Sounder. Currently, these instruments are aboard five polar-orbiting satellites, namely, NOAA-18, NOAA-19, Metop-A, Metop-B, and Suomi-NPP. The SFR algorithm relies on a separate snowfall detection algorithm that is composed of a satellite-based statistical model and a set of numerical weather prediction model-based filters. There are four components in the SFR algorithm itself: cloud properties retrieval, computation of ice particle terminal velocity, ice water content adjustment, and the determination of snowfall rate. The retrieval of cloud properties is the foundation of the algorithm and is accomplished using a one-dimensional variational (1DVAR) model. An existing model is adopted to derive ice particle terminal velocity. Since no measurement of cloud ice distribution is available when SFR is retrieved in near real time, such distribution is implicitly assumed by deriving an empirical function that adjusts retrieved SFR toward radar snowfall estimates. Finally, SFR is determined numerically from a complex integral. The algorithm has been validated against both radar and ground observations of snowfall events from the contiguous United States with satisfactory results. Currently, the SFR product is operationally generated at the National Oceanic and Atmospheric Administration and can be obtained from that organization.

1. Introduction

Satellite remote sensing of snowfall is challenging due to the complexity of atmospheric processes involved and the lack of both the understanding about these processes and the information on many related variables. It is more difficult to estimate snowfall than rainfall because more information, such as ice particle shape and density, is required for developing physically based algorithm and generally unavailable. Consequently, studies on snowfall retrieval have lagged significantly behind the development of satellite rain rate algorithms [*Ferraro and Marks*, 1995; *Evans et al*., 1995; *Bauer and Bennartz*, 1998; *Weng et al*., 2003; *Ferraro et al*., 2005; *Kummerow et al*., 2011]. However, snowfall retrieval from passive microwave (PMW) instruments has been gaining momentum in recent years. The observations from PMW are uniquely suitable for snowfall detection and retrieval [*Kongoli et al*., 2003; *Bennartz and Bauer*, 2003; *Skofronick-Jackson et al*., 2004; *Noh et al*., 2006; *Kim et al*., 2008; *Liu and Seo*, 2013; *Skofronick-Jackson et al*., 2013; *You et al*., 2017]. PMW has the ability to penetrate clouds hence directly bearing the signal of snow particles. High frequencies above 150 GHz, such as window channels around 160 GHz and water vapor sounding channels around 183 GHz, are particularly sensitive to the radiance depressing effect of ice scattering. Some land snowfall rate algorithms have been developed utilizing this property and are briefly reviewed in this section. It is noted that essentially all the current passive microwave algorithms that retrieve precipitation (rainfall or snowfall) over land rely on the sensing of ice signature.

Skofronick-Jackson et al. [2004] developed a physically based snowfall rate model using high-frequency PMW observations from the Advanced Microwave Sounding Unit-B (AMSU-B) radiometer. They generated snow, temperature, and relative humidity profiles using the Mesoscale Model cloud model and input the modeled profiles and estimated surface emissivity to a radiative transfer model (RTM) to simulate AMSU-B brightness

temperatures (T_bs) at five frequencies. In the RTM, snow particles were assumed to be a concatenation of equivalent ice spheres. Three model parameters, respectively, controlling snow mass, surface emissivity, and relative humidity were systematically adjusted to obtain a large set of snow cloud profiles. The algorithm retrieved snow parameters are the ones with computed T_bs that best match the observations at all five frequencies. The model was applied to a case study, and the retrieved snow mass was shown to be consistent with the corresponding radar reflectivity. Their study demonstrated that high-frequency PMW measurements can provide information on snowfall over land. It also emphasized the importance of microphysics measurements for accurate snowfall retrieval and the lack of such data.

Noh et al. [2006] developed a Bayesian snowfall rate algorithm for AMSU-B. They built the a priori database required by the algorithm using an RTM and airborne and surface-based radar data collected from areas around the Japan Sea. A notable feature of the algorithm is that scattering properties of nonspherical ice particles were used in the RTM to construct the a priori database. The Bayesian algorithm was applied to three snowfall cases that occurred in the vicinity of the Japan Sea. The correlation coefficient between 1° × 1° gridded AMSU-B snowfall rate and radar snow accumulation ranges from 0.6 for light snowfall to an impressive 0.96 for heavy snowfall. The authors noted that there is a negative correlation between the amount of liquid water in the snowing clouds and the correlation coefficient. In addition, the snowfall rate algorithm is only applicable to the areas where the airborne and radar data used for building the a priori database were collected.

Kim et al. [2008] incorporated several improvements in the physical snowfall model described in *Skofronick-Jackson et al.* [2004] for AMSU-B. Some major improvements included the capability to compute and utilize single scattering properties of various nonspherical ice particle shapes in RTM calculation, to adopt in situ observation-based snow particle size distributions and to optimize retrievals with a Bayesian model as well as considering T_b error covariance in the model. The updated algorithm was applied to the same snowfall case as used in the original study and showed better consistency with radar reflectivity than the original algorithm.

Liu and Seo [2013] took a statistical approach to develop a snowfall detection algorithm for AMSU-B and Microwave Humidity Sounder (MHS). They trained the radiometer measurements using CloudSat detected snowfall (defined as reflectivity ≥ -15 dBZ) and created a snowfall look-up table (LUT). The satellite data at five frequencies higher than 89 GHz were transformed to three principal components from the empirical orthogonal function analysis and formed the three axis of the LUT. Each element of the LUT represented snowfall probability defined as the number ratio of snowfall pixels and all data pixels. CloudSat-retrieved snowfall rate data have also been used to train a snowfall rate algorithm for the Global Precipitation Measurement (GPM) Microwave Imager (GMI). A major factor motivating these previous authors to adopt the statistical method was that their research revealed a "warming" signal in high-frequency T_bs in most snowfall rather than cooling. They believed that emission was the main reason for the warming and it was inadequate to solely rely on the scattering effect to detect snowfall.

Kummerow et al. [2015] presented the Goddard profiling (the GPROF) 2014 precipitation algorithm for GMI. It is a fully parametric Bayesian algorithm over all surface types without using explicit rainfall screening procedure. The a priori database for the land portion of the algorithm was mostly constructed using National Mosaic and Multi-Sensor Quantitative Precipitation Estimation (NMQ) project [*Zhang et al*., 2011] radar data and the collocated overpasses of the GPM constellation members (V03). It is noted that the database has since been updated using primarily the GPM Dual-frequency Precipitation Radar-retrieved precipitation (V04). The database was divided into subsets based on land surface temperature, total precipitable water (TPW), and surface type. Each surface type was assumed to have self-similar emissivity [*Aires et al*., 2011], and a total of 14 surface types was used. The GPROF 2014 algorithm can retrieve both rainfall and snowfall utilizing ancillary data to differentiate between precipitation types. It should be noted that the GPROF V03 for the MHS, Advanced Technology Microwave Sounder (ATMS) and Sounder for Probing Vertical Profiles of Humidity (SAPHIR) are all based upon a NASA Multi-scale Modeling Framework-derived single (surface-blind) database that retrieve snowfall directly from the observations [*Kidd et al*., 2016]. The GPROF V04 for MHS/ATMS/SAPHIR uses scan-angle interpolation during retrieval.

You et al. [2015] described a prototype land precipitation algorithm for the Special Sensor Microwave Imager/Sounder (SSMI/S). The a priori database of the Bayesian algorithm was developed from collocated

NMQ radar precipitation data and SSMI/S observations (as the first three principal components of the T_bs). The main purpose of the study was to examine the effect of using a single database on a Bayesian retrieval algorithm versus using databases stratified by a set of ancillary parameters. Compared to using a single database, *You et al.* [2015] demonstrated that significant improvement could be achieved with rainfall and snowfall detection and rate retrieval when databases were stratified by surface and cloud parameters. Conceptually, the improvement could be attributed to the fact that each stratified database contains profiles with more homogeneous surface and atmospheric conditions and hence can better represent the precipitation structure for a given set of SSMI/S observations.

The algorithm introduced here employs a one-dimensional variational (1DVAR)-based approach to retrieve snowfall rate (hereafter denoted as SFR to represent the algorithm developed in this study) over land. The required input is measurements from polar-orbiting PMW instruments that have appropriate high-frequency sounding channels. It is different from the above mentioned algorithms in that it relies on model physics to cover a wide range of snowfall conditions rather than utilizing an a priori database or LUT. It is noted that there are also some statistical elements in the SFR algorithm such as its calibration using radar snowfall estimates (section 3.2) due to the lack of information on the structures of snowing clouds. Currently, the SFR product is operational at National Oceanic and Atmospheric Administration (NOAA)/National Environmental Satellite, Data, and Information Service (NESDIS). Historical SFR data can be obtained from NOAA Comprehensive Large Array-data Stewardship System (CLASS). Section 2 describes the satellite instruments and their measurements as input to the SFR algorithm. The 1DVAR model and an ice particle terminal velocity model are also introduced in this section. The SFR algorithm including a set of snowfall detection filters and the snowfall rate component are detailed in section 3. The results of a validation study and a series of error analyses are presented in section 4. Finally, section 5 summarizes the study and provides final conclusions.

2. Data and Model

2.1. Instruments and Data

The SFR algorithm described here utilizes measurements from two sets of PMW instruments: Advanced Microwave Sounding Unit-A (AMSU-A) and Microwave Humidity Sounder (MHS) pair, and the Advanced Technology Microwave Sounder (ATMS). The first satellite that carries AMSU-A and MHS is NOAA-18, a satellite in the NOAA Polar Operational Environmental Satellites (POES) program. Since the launch of NOAA-18 in 2005, three more satellites have been put in orbit with these sensors on board, i.e., POES NOAA-19, and the European Organisation for the Exploitation of Meteorological Satellites (EUMETSAT) Metop-A and Metop-B. Currently, ATMS is only aboard the Suomi-NPP although future Joint Polar Satellite System (JPSS) satellites will also carry this instrument. AMSU-A and MHS combined have 20 channels ranging from 23.8 GHz to 190.31 GHz with different beam widths (Table 1). ATMS has similar frequency range but adds two additional frequencies (Table 1). They are divided into three groups: temperature sounding, water vapor sounding, and window channels. Among them, the high-frequency window and water vapor channels at 89/88.2 GHz and above are particularly sensitive to precipitation sized ice particles and can be employed for snowfall rate retrieval. These sensors are cross-track scanning radiometers with variable footprint size across scan line. AMSU-A has 30 observations on each scan line, MHS has 90, and ATMS has 96.

The T_bs from the above mentioned radiometers are the main input data to the SFR algorithm and can be obtained from NOAA CLASS. In addition, the algorithm also requires certain environmental state variables, such as temperature and relative humidity profiles, provided by a numerical weather prediction (NWP) model. The model employed in the current algorithm is the Global Forecast System (GFS) data downloadable from NOAA National Operational Model Archive and Distribution System (NOMADS). In NOAA operation, these input data are made available in near real time through NOAA internal data feed to ensure that the SFR latency can meet the operational requirements.

2.2. Radiative Transfer Model and Variational Inversion Method

A 1DVAR approach [*Yan et al.*, 2008] is used in the SFR algorithm to retrieve cloud properties. The original model was developed to retrieve ice cloud properties and snow emissivity at five AMSU microwave window channels: 23.8, 31.4, 50.3, 89, and 150 GHz. Among them, the 50.3 GHz is not used in the SFR algorithm because (i) this frequency is difficult to simulate accurately and (ii) it holds much less information about

Table 1. AMSU/MHS and ATMS Channels Comparison[a]

AMSU/MHS				ATMS			
Ch	GHz	Beam Width(deg)	Pol	Ch	GHz	Beam Width(deg)	Pol
1	23.8	3.3	QV	1	23.8	5.2	QV
2	31.399	3.3	QV	2	31.4	5.2	QV
3	50.299	3.3	QV	3	50.3	2.2	QH
				4	51.76	2.2	QH
4	52.8	3.3	QV	5	52.8	2.2	QH
5	53.595 ± 0.115	3.3	QH	6	53.596 ± 0.115	2.2	QH
6	54.4	3.3	QH	7	54.4	2.2	QH
7	54.94	3.3	QV	8	54.94	2.2	QH
8	55.5	3.3	QH	9	55.5	2.2	QH
9	*fo* = 57.29	3.3	QH	10	*fo* = 57.29	2.2	QH
10	*fo* ± 0.217	3.3	QH	11	*fo* ± 0.3222 ± 0.217	2.2	QH
11	*fo* ± 0.3222 ± 0.048	3.3	QH	12	*fo* ± 0.3222 ± 0.048	2.2	QH
12	*fo* ± 0.3222 ± 0.022	3.3	QH	13	*fo* ± 0.3222 ± 0.022	2.2	QH
13	*fo* ± 0.3222 ± 0.010	3.3	QH	14	*fo* ± 0.3222 ± 0.010	2.2	QH
14	*fo* ± 0.3222 ± 0.0045	3.3	QH	15	*fo* ± 0.3222 ± 0.0045	2.2	QH
15	89.0	3.3	QV				
16	89.0	1.1	QV	16	88.2	2.2	QV
17	157.0	1.1	QV	17	165.5	1.1	QH
18	183.31 ± 1	1.1	QH	18	183.31 ± 7	1.1	QH
19	183.31 ± 3	1.1	QH	19	183.31 ± 4.5	1.1	QH
20	190.31	1.1	QV	20	183.31 ± 3	1.1	QH
				21	183.31 ± 1.8	1.1	QH
				22	183.31 ± 1	1.1	QH

[a]QV: quasi-vertical polarization and QH: quasi-horizontal polarization.

snowfall than some other frequencies. In addition, a frequency (190.3 GHz for MHS and 183 ± 7 GHz for ATMS) was added to the RTM for snowfall retrieval (section 3.2) due to its sensitivity to snowfall signal. The inversion method involves a set of iterations where T_bs at the five frequencies are simulated using an RTM [*Weng et al*., 2001; *Yan et al*., 2008] at each iteration with given atmospheric and surface parameters (i.e., control vector). The differences between simulated and observed T_bs (ΔT_bs) are compared to preset thresholds. The iteration will terminate if the ΔT_bs fall below the acceptable thresholds, indicating that the retrieval converges. Otherwise, the elements of the control vector are adjusted and iteration will continue until it reaches the maximum allowed number of iteration, indicating that the retrieval is nonconvergent. The threshold for the first five frequencies is 1.5 K and for 190.3/183 ± 7 GHz is 3 K. The atmospheric and surface parameters from a successful run become the retrieved properties using the inversion method. The parameters include land surface emissivity at the six frequencies, total precipitable water (TPW), ice water path (I_w), effective size of ice particles (D_e), surface temperature (T_s), and cloud temperature (T_c).

The RTM utilized in this 1DVAR algorithm is a two-stream, one-layer model [*Weng et al*., 2001]. Simulation error caused by the simplifications is mitigated by a correcting procedure developed by *Weng and Grody* [2000]. Simulated T_bs are corrected with a set of empirical equations that were derived from a data set of T_b observations and the corresponding uncorrected simulations. According to *Yan et al.* [2008], the standard deviations of the corrected T_bs at frequencies 23.8, 31.4, 89, and 150 GHz are 0.21, 0.33, 0.72, and 0.68 K, respectively. Additional study shows that the standard deviation for 190.31 GHz and 183 ± 7 GHz are 4.06 and 2.62 K, respectively.

This 1DVAR model was utilized in the SFR algorithm for a few reasons. While a simple assumption of one-layer atmosphere is made in the RTM, it allows the model parameters, such as ice water path, to be expressed in analytic forms and provides one with both qualitative and quantitative understanding of the connection among model parameters. The two-stream formula makes computation effective so retrieval can be completed quickly even with full-orbit data. Computation efficiency and product latency can be important factors for operational applications such as weather forecasting. Lastly, the 1DVAR model was developed for retrieving snow emissivity; hence, its parameterization, such as bias correction and emissivity initialization, is

consistent with emissivity properties of cold conditions. The close connection between snow emissivity and snowfall makes the 1DVAR an appropriate model to use in a snowfall rate algorithm.

2.3. Ice Particle Terminal Velocity

An important component of the SFR algorithm is the ice particle terminal velocity. *Heymsfield and Westbrook* [2010] modified *Mitchell*'s [1996] formula for ice particle fall speed and developed a new equation:

$$V(D) = \frac{\eta \delta_0^2}{4\rho_a D}\left[\left(1+\frac{4\sqrt{X}}{\delta_0^2\sqrt{C_0}}\right)^{1/2}-1\right]^2, \quad (1)$$

where V is ice particle terminal velocity, D the maximum dimension of the ice particle, η dynamic viscosity of air, ρ_a air density, δ_0 and C_0 are fitting parameters, $\delta_0 = 8.0$ and $C_0 = 0.35$, and the modified Best number X is defined as

$$X = \frac{8mg\rho_a}{\pi\eta^2\sqrt{A_r}}, \quad (2)$$

where m is mass, $m=\pi D^3\rho_i/6$ for spherical particles, ρ_i density of ice particle and assumed to be 0.6 g/cm^3, g the standard gravity, and A_r the ice particle area ratio (the area of the particle projected normal to the flow divided by the area of a circumscribing disc) and is 1 for spherical particle.

Heymsfield and Westbrook [2010] computed terminal velocities of ice particles in various shapes using this approach and compared with measurements. Their results show that the predicted and the measured particle fall velocities agree well for all particle shapes examined. This conclusion is the basis for selecting the *Heymsfield and Westbrook* [2010] model to compute ice particle terminal velocity in the SFR algorithm.

3. Methodology

The SFR algorithm consists of two main components: snowfall detection (hereafter denoted as SD to represent the algorithm embedded in SFR) and snowfall rate. They are essentially two independent algorithms. The former is a statistical model, while the latter is physically based. The focus here is on the introduction of the snowfall rate component, although descriptions of a set of snowfall filters will also be given since they are part of the SD algorithm and have only been briefly mentioned previously [*Foster et al*., 2012].

3.1. Snowfall Detection

Snowfall detection is an integral part of the snowfall rate retrieval. Only when snowfall is detected at a field of view (FOV) will the SFR algorithm be applied to retrieve snowfall rate. There are two elements in the SD algorithm: a logistic regression-based statistical model [*Kongoli et al*., 2015] and a set of filters based on NWP model data.

3.1.1. Statistical Snowfall Detection Model

The statistical SD model is detailed in *Kongoli et al.* [2015] and briefly described here for completeness. The model derives the probability of snowfall from the principal components of the microwave frequencies at and above 89 GHz, i.e., seven frequencies for ATMS and five for MHS (section 2.1). The logistic regression SD model was trained using collocated satellite data and ground observations. Two sets of model coefficients were derived, each for a certain temperature regime, because the high frequencies respond differently to snowfall in relatively "warm" atmosphere versus under very cold conditions. The temperature sounding channel at 53.6 GHz is taken as a proxy of the atmospheric temperature and is used to define the two regimes. Statistical analysis was conducted to establish optimal probability thresholds for snowfall occurrence.

3.1.2. Snowfall Filters

Both rainfall and snow cover can cause similar responses in microwave measurements as snowfall. Therefore, they can contaminate the outcome of the statistical SD model. This consideration led to the development of a set of filters to further screen the "snowfall" identified by the SD model. The filters use atmospheric and surface information from the GFS, the global operational NWP model at NOAA's National Centers for Environmental Prediction (NCEP). The reason for using NWP forecast instead of analysis data is that the SFR product is generated in near real time at NOAA/NESDIS which requires timely data input. The GFS model runs four times daily and generates forecast out to 192 h at 3 h increment.

The first filter checks 2 m temperatures, T_{2m}, at the two consecutive GFS forecast times that encompass the satellite passing time. If both temperatures are above 1°C, it indicates a persistently warm environment at the surface that generally cannot sustain snowfall. The second filter checks T_{2m} and the maximum of the atmospheric temperature profile, T_{max}, and compares them with their respective thresholds at 1°C and 0.5°C. The algorithm searches for T_{max} starting from one model level above the surface level and up. Therefore, T_{2m} and T_{max} are mutually exclusive. Warm layers in the atmosphere can result in freezing rain or mixed precipitation at the surface. These conditions can cause complicated responses in satellite measurements and lead to large bias in a scattering-based snowfall algorithm like SFR. This filter is designed to eliminate precipitation phases other than snowfall. The threshold for T_{2m} was selected based on analysis of ground observed T_{2m} during snowfall. The analysis revealed that only a small percentage of T_{2m} exceeded 1°C. For instance, only 4% of the T_{2m} associated with snowfall is above 1°C in the in situ data used to develop the ATMS SD algorithm. Raising this temperature threshold will increase the risk of elevated false alarm rate in identified snowfall. The 0.5°C threshold for T_{max} is a conservative adaptation of a snowfall criterion used at some National Weather Service Weather Forecasting Offices (B. Carcione, personal communication, NWS, 2014). The criterion requires T_{max} to be less than 1°C and was derived from the results of several studies on freezing precipitation [*Rauber et al*., 2001a, 2001b; *Stewart and King*, 1987].

The most important filter is a check on cloud thickness. The current algorithm requires cloud thickness to be at least 1500 m to pass this filter. While this requirement is likely to remove shallow snowfall such as lake effect snow, it will not significantly lower the Probability of Detection (POD). This is because the SFR algorithm is not sensitive to very shallow snowfall due to the weak effect from the latter on microwave measurements. The exertion of a cloud thickness threshold eliminates most of the confusions between true snowfall and snow cover on the surface. Our analysis has shown that this is a very effective filter that can significantly reduce false snowfall detection.The GFS relative humidity (RH) profile is utilized to determine cloud thickness. An atmospheric level is considered to have a cloud if RH is at or above 89%. This threshold is consistent with the critical RH (RH_c) used in the GFS microphysics scheme (S. Moorthi, personal communication, NOAA/NCEP, 2011):

$$RH_c = 0.85 + 0.1499w \tag{3}$$

where

$$w = -0.1529^{*}\left[\ln\left(\frac{\cos(\theta)}{n_x{}^{*}n_y}\right) + 9.8008\right]$$

where θ is latitude, n_x is dimension of the GFS in the latitude direction, and n_y is dimension of the GFS in the longitude direction. For 1° GFS, 89% is a representative RH_c for midlatitude.

Cloud thickness is an accumulation of all atmospheric levels where RH is at or above 89% up to 5 km regardless of single-layer or multilayer clouds. All channels utilized in the algorithm peak below this maximum height. In addition, the base of snowing cloud usually extends well below 5 km. There are potential cases where each layer of a multilayer cloud is less than 1.5 km thick, but the combined layers can satisfy this criterion. However, since the maximum height is set at 5 km, a combined cloud thickness greater than 1.5 km below this level is still a substantial existence of clouds and can produce snowfall. It is noted that this check is but one of several checks in the algorithm and is a necessary but not sufficient condition for the existence of snowfall. This filter will eliminate some legitimate but shallow snowfall such as lake effect snow. However, passive microwave measurements are intrinsically insensitive to this type of snowfall so the filter does not impose a significant impact on the POD.

The current SD algorithm is limited to detecting snowfall when the limb corrected 53.6 GHz is higher than 240 K. Based on the empirical equation in Figure 1 of *Kongoli et al.* [2015], this low limit corresponds to about −14°C/7°F in 2 m air temperature. There is no temperature upper limit for retrieval except the temperature-related criteria that is part of the SD algorithm. This temperature range allows snowfall rate retrieval over the majority of the globe and an overwhelming portion of the contiguous United States (CONUS) throughout the winter season regardless of whether there is snow cover on the ground. A very cold atmosphere usually does not contain enough water vapor that can provide the necessary emission

to mask the surface. Consequently, measurements from the water vapor sounding channels are often contaminated by the surface under such conditions. Even the 157 GHz (MHS) and 165.5 GHz (ATMS), which are sensitive to both the atmosphere and the surface, have different characteristics under cold and dry conditions versus when the atmosphere is relatively warm and moist. Since the SD algorithm relies on water vapor to separate in-cloud snow from snow cover on the surface, the changes in channel measurements make it difficult to apply the current algorithm in very cold environments, i.e., limb corrected 53.6 GHz less than 240 K. Additional data sources and/or framework will have to be used to develop a cold weather SD algorithm.

3.2. Snowfall Rate

The snowfall rate component of the SFR algorithm is more physically based on its formulation than the snowfall detection approach. From *Yan et al.* [2008] and *Weng et al.* [2001], the particle distribution function (PDF) of ice particles with a modified gamma distribution is

$$N(D) = \frac{\mathrm{N}_0 D^{\nu-1} e^{-D/D_m}}{\Gamma(\nu) D_m^{\nu}}, \tag{4}$$

where D is the diameter of the ice particle (assuming spherical habit), D_m the typical diameter of the particle, N_0 the total number of particles, ν the shape parameter for the gamma distribution, and Γ the gamma function. Furthermore,

$$D_m = D_e \frac{\Gamma(\nu)}{\Gamma(\nu - 1)} \tag{5}$$

and

$$N_0 = \frac{6\mathrm{I}_w \Gamma^3(\nu + 1)}{\pi \rho_l D_e^3 \Gamma(\nu + 3)\Gamma^2(\nu)}, \tag{6}$$

where D_e is the effective diameter of the ice particles and I_w ice water path. If the shape parameter is assumed to be 1, the PDF in equation (4) reduces to an exponential distribution:

$$N(D) = \frac{\mathrm{I}_w e^{-\frac{D}{De}}}{\pi \rho_l D_e^4}. \tag{7}$$

With the assumption that the number of ice particles follows the above exponential distribution, the unadjusted (explained in text below) water equivalent snowfall rate, SFR_u, can be expressed as follows:

$$\mathrm{SFR}_u = \int_0^{\infty} \frac{\pi \rho_l D^3 N(D) V(D)}{6\mathrm{H}\rho_w} \mathrm{d}D \tag{8}$$

or

$$\mathrm{SFR}_u = \frac{I_w}{6\mathrm{H}\rho_w D_e^4} \int_0^{\infty} D^3 e^{-\frac{D}{De}} V(D) \mathrm{d}D \tag{9}$$

where H is cloud thickness and ρ_w the density of water. By adopting the Heymsfield and Westbrook's model (equations (1) and (2)) and assuming spherical ice habit, SFR_u can be derived as follows:

$$\mathrm{SFR}_u = \frac{I_w \eta \delta_0^2}{24\mathrm{H}\rho_w \rho_a D_e^4} \int_0^{\infty} D^2 e^{-D/D_e} \left[\left(1 + \frac{8D^{3/2}}{\eta \delta_0^2} \sqrt{\frac{g\rho_l \rho_a}{3C_0}} \right)^{1/2} - 1 \right]^2 \mathrm{d}D. \tag{10}$$

An implicit assumption is made in the above equation, i.e., ice water content (IWC) is uniformly distributed in the cloud column. It is consistent with the two-stream RTM [*Yan et al.*, 2008]. However, this assumption is not a true representation of cloud physics. In snowing clouds, ice crystals grow in mass as they fall in the cloud through Bergeron process, i.e., supercooled water vapor deposition, or through accretion (riming), i.e., freezing of super cooled liquid droplets onto the surface of ice crystals. These mechanisms generally lead to higher IWC at the lower portion of the cloud than in the upper portion. For instance, Figure 1 presents 10 randomly selected, normalized IWC estimate profiles retrieved from CloudSat [*Stephens et al.*, 2002]. In general, these profiles show an increasing trend from cloud top to

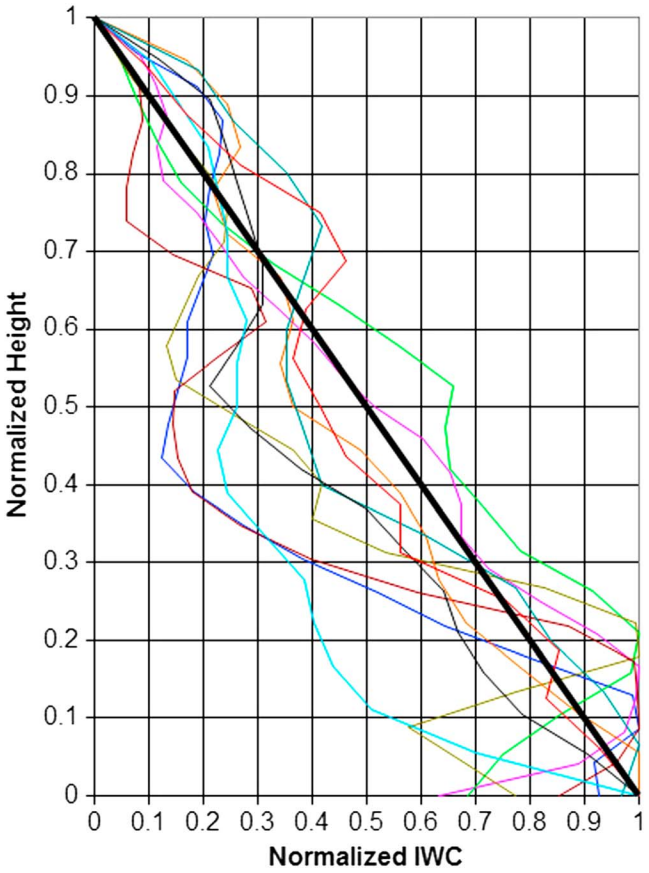

Figure 1. CloudSat derived ice water content (IWC) profiles. The values have been normalized.

cloud base and supports the notion that IWC is not uniformly distributed in cloud. To mitigate the effect of the simplistic assumption about IWC, an adjusting factor α is introduced so the final SFR equation is as follows:

$$\mathrm{SFR} = \mathrm{A}\int_0^\infty D^2 e^{-D/D_e}\left[\left(1+BD^{3/2}\right)^{1/2}-1\right]^2 dD \tag{11}$$

where

$$A = \frac{\alpha I_w \eta \delta_0^2}{24 \mathrm{H} \rho_w \rho_a D_e^4} \tag{12}$$

$$B = \frac{8}{\eta \delta_0^2}\sqrt{\frac{g\rho_l \rho_a}{3C_0}}. \tag{13}$$

Since equation (11) does not have an analytical solution, it is solved numerically using Romberg's method. Factor α is estimated by spatially and temporally matching SFR_u with the Stage IV [*Lin and Mitchell*, 2005] precipitation data (http://www.emc.ncep.noaa.gov/mmb/ylin/pcpanl/stage2/) and adjusting toward the latter. Stage IV is a Next Generation Weather Radar and gauge combined hourly precipitation product generated by National Oceanic and Atmospheric Administration (NOAA)/National Centers for Environmental Prediction (NCEP). Figure 2 shows ATMS SFR_u bias from Stage IV using ATMS retrieval from four snowfall events in the contiguous United States (CONUS). The events occurred on 19–20 December 2012 in the western region to the Midwest, 26 December 2012 in the Midwest to the East Coast, 21 February 2013 in the Midwest, and 5–6 March 2013 in the Midwest to the Mid-Atlantic Region. Most snowfall was from synoptic systems and ranged from light to heavy in intensity across the snow areas. A linear relationship between SFR and SFR_u, i.e., a constant α was derived based on the plot. This is equivalent to assuming that the ratio between the average IWC in the cloud column and the "effective IWC," IWC_e, is a constant. SFR can be conceptually expressed as the product of IWC_e and ice particle fall velocity, *V*. While this approach results in good correlation between SFR and Stage IV, the bias indicates a clear underestimation in the SFR product. To reduce the bias, the ATMS and MHS SFR products were further calibrated against the Multi-Radar Multi-Sensor (MRMS) radar instantaneous snowfall rate data [*Zhang et al.*, 2016] (http://mrms.ou.edu/) developed at the NOAA/National

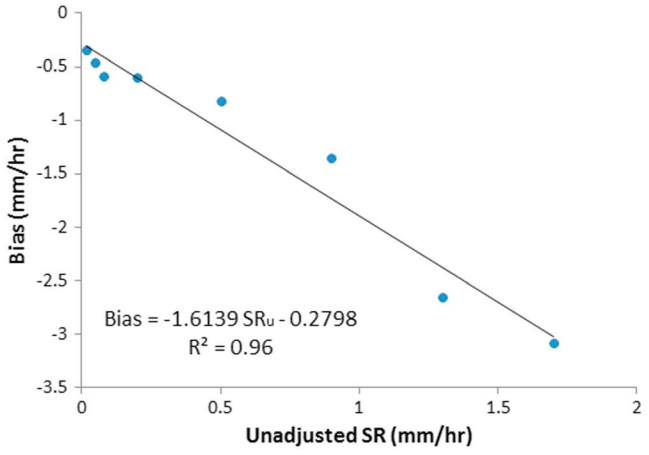

Figure 2. Bias of unadjusted MHS snowfall rate from Stage IV hourly precipitation data.

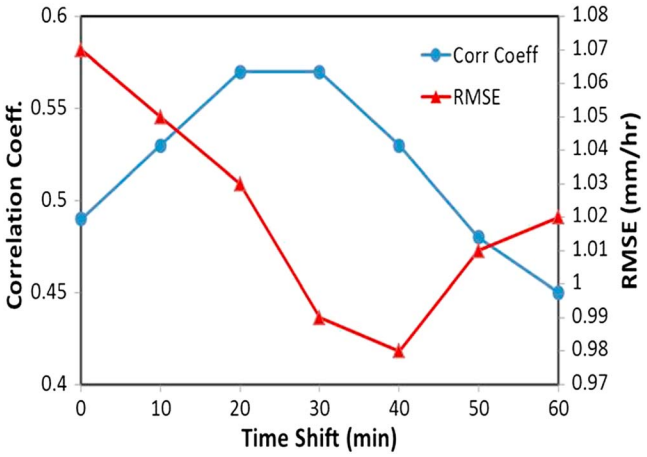

Figure 3. Statistics between ATMS SFR and MRMS snowfall rate estimates as function of time shift between the two (satellite first). The plot reveals that the two sets of data are best correlated with a 30 min time shift.

Severe Storms Laboratory (NSSL). The radar estimates were collocated with satellite retrievals in space through convolution and in time with a 30 min shift. As a measure of quality control, only the MRMS data with the Radar QPE Quality Index at or greater than 0.5 were used based on the recommendation of a MRMS developer (J. Zhang, personal communication, NSSL, 2014). Analysis has shown that the maximum correlation between the two sets of data has a time shift (Figure 3). This is due to the fact that the measurements of microwave sensors integrate the combined effect from the entire precipitation layer, while radar precipitation is usually derived from the base reflectivity. The height difference compounded with the relatively slow terminal velocity of snow particles gives rise to the time shift shown in Figure 3. For calibration, a satellite and radar collocated data point is selected only if more than 90% of a snowing FOV (SFR $>$ 0) is filled with radar pixels that are snowing. It is also required that no radar pixel in the FOV is rain. Such stringent criteria were set to ensure the quality of the calibration data. By histogram matching the collocated data following the approach described in *Kidder and Jones* [2007], the final adjusting function (instead of a single factor) for ATMS SFR_u is derived:

$$SFR = 2.98SFR_u - 0.48SFR_u^2 + 0.06SFR_u^3 \quad (14)$$

For MHS SFR_u:

$$SFR = 3.22\ SFR_u - 0.39SFR_u^2 + 0.04SFR_u^3. \quad (15)$$

Figure 4 compares the probability distribution functions (PDFs) of ATMS SFR versus MRMS instantaneous snowfall rate and MHS SFR versus MRMS instantaneous snowfall rate before and after histogram matching. Before the adjustment, both the ATMS SFR and the MHS SFR have more very light snowfall (~0.2 mm/h) than

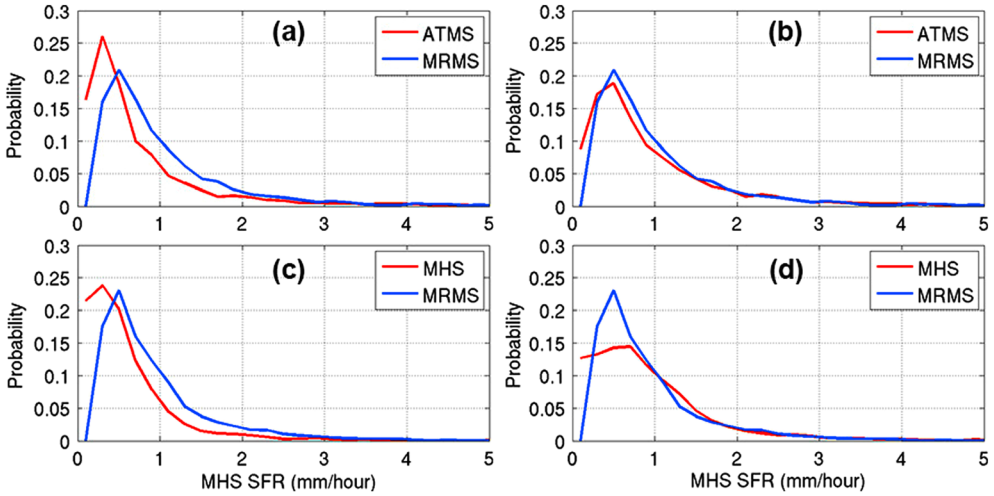

Figure 4. PDFs of ATMS SFR and the matching MRMS instantaneous snowfall rate (a) before histogram matching and (b) after histogram matching, and PDFs of MHS SFR and the matching MRMS instantaneous snowfall rate (c) before histogram matching and (d) after histogram matching.

Table 2. Calibration Statistics of the SFR Algorithm

	Correlation Coefficient	Bias (mm/h)	RMS (mm/h)
ATMS	0.55	−0.03	0.67
MHS	0.47	−0.03	0.74

MRMS but not enough snowfall between 0.5 mm/h and 2–3 mm/h (Figures 4a and 4c). The histogram matching effectively reduces such discrepancy for ATMS SFR so its PDF agrees much better with that of MRMS (Figure 4b). However, the adjustment of MHS PDF is less than satisfactory at the low end (<1 mm/h) (Figure 4d). Much more MRMS snowfall rate data fall around 0.5 mm/h than MHS SFR. The difference is balanced out by having more MHS data lower than about 0.2 mm/h and around 1.5 mm/h than MRMS data. Table 2 gives the calibration statistics for both ATMS and MHS SFRs. The advantage of ATMS over MHS for snowfall rate retrieval is reflected in the higher ATMS correlation coefficient at 0.55 versus MHS 0.47 and lower ATMS RMS at 0.67 mm/h versus MHS 0.74 mm/h. Both have the same low bias of −0.03 mm/h. The ATMS SD also showed more skill than MHS SD in our previous studies (results not shown). It is conceivable that the algorithm is optimized for CONUS since the adjustment was based on the MRMS data which is limited to this region. However, it should be pointed out that the cloud properties are retrieved from the 1DVAR and is independent of the radar data. The correlation between SFR before and after the adjustment essentially remains unchanged. The main purpose of the radar-based adjustment is to reduce the bias caused by the assumption about IWC profile.

Other variables in equations (11)–(13) are as follows: η, H, and ρ_a are derived from GFS, ρ_w is 1000 kg/m^3, ρ_I is set at 600 kg/m^3, and I_w and D_e are retrieved using the 1DVAR described in section 2.2. The original model was modified for MHS and ATMS, respectively. An additional channel, 190 GHz (183 ± 7 GHz), was added to the RTM for MHS (ATMS). The weighting function of this water vapor sounding channel peaks higher than the 157 GHz (165.5 GHz) and can complement the latter by pulling in more information about in-cloud snowfall. It is the most sensitive channel to precipitation among the water vapor sounding channels in MHS (ATMS). Including this channel in the RTM helps to improve the retrieval accuracy of the cloud properties. In the original 1DVAR, TPW and T_s are retrieved variables. However, these quantities are derived from GFS and are fixed in the SFR algorithm in an effort to reduce the size of the control vector.

Brightness temperatures at window channels are closely modulated by surface emissivity. If there is not enough water vapor in the atmosphere, even some water vapor sounding channels with low peaking weighting functions, such as 183 ± 7 GHz, can be under significant influence from the surface. However, snow emissivity is highly variable and dependent on many factors including snow age, snow depth, snow water content, and incident angle [*Yan et al.*, 2008]. Much of the state information required to directly compute snow emissivity is not readily available. One of the major advantages of adopting the 1DVAR approach to derive cloud properties is that it simultaneously retrieves emissivity. This ensures that all retrieved variables are physically consistent and reconcilable in the framework of the two-stream radiative transfer model. It also eliminates the need for a priori knowledge of the land surface types and their emissivity. The SFR algorithm is applicable to all land surfaces including snow cover.

The SFR algorithm runs for all satellite FOVs where snowfall is detected by the SD algorithm. The 1DVAR converges in about 90% cases based on analysis (section 4.2.4). Nonconvergence generally occurs when snowfall signal is very weak or very strong and indicates inadequate initialization of the control vector. Currently, the nonconvergent retrievals are included in the SFR product since they usually contain some useful information such as the existence of snowfall and the range of snowfall intensity. Further study is needed to reduce the occurrences of nonconvergence.

4. Validation and Error Analysis

4.1. Validation

The SFR algorithm was validated against both radar estimates and gauge observations. A SFR validation study was conducted using data collected from several multiday snowfall events in CONUS in winter 2013–2014 and winter 2014–2015 (Table 3). These were different events from those used for algorithm calibration. The satellite-retrieved product was collocated with MRMS instantaneous snowfall rate data by convolving MRMS pixels to the satellite FOVs. As discussed above, there is a 30 min time shift between satellite observations and the collocated MRMS data for better data compatibility (section 3.2). Figure 5 compares the PDFs of ATMS SFR and MRMS instantaneous snowfall rate estimates and those of MHS SFR and MRMS estimates.

Table 3. Validation Events

Event Number	Date	Event Type
1	21–22 January 2014	Moderate to strong nor'easter in the Mid-Atlantic Region
2	28–29 January 2014	Significant snowstorm mostly impacting the southeast states
3	2–4 February 2015	Light-moderate event in the Midwest
4	16–17 February 2015	Cross-country (Colorado to Mid-Atlantic) major snowstorm
5	20–22 February 2015	Two events: Event 1: Light snowfall in the Rockies, Event 2: Intense snowstorm from Midwest to Mid-Atlantic to northeast
6	26 February 2015 to 1 March 2015	Light to moderate snowfall from Colorado to Midwest

ATMS and MRMS generally agree well with the former having slightly more light snowfall around 0.5 mm/h and below and less medium to intense snowfall than MRMS above 1 mm/h (Figure 5a). The MHS validation PDF shows similar pattern as for calibration for light snowfall but with much better agreement with MRMS. It is noted that the criteria for collocating SFR and MRMS are different for calibration (section 3.2) and validation. Specifically, the requirement for 90% radar coverage within a FOV was removed when building the validation data set. This is due to the consideration that validation should cover all cases where SFR $>$ 0 regardless of radar coverage within the FOVs. Such statistics are more representative of the algorithm performance and are more meaningful to users. However, the requirement about no raining radar pixel in a satellite FOV still remained. This change explains the fact that there is much more light snowfall in the validation data than in the calibration data (Figures 5 and 4). Figure 6 displays the scatterplots of MRMS snowfall rate versus ATMS SFR and MRMS versus MHS SFR. Data are grouped and averaged in 0.2 mm/h bins. The colors represent data density. The collocated ATMS data show better tendency to follow the 1:1 line than the MHS data does which signals a higher correlation. The ATMS data also display less scattering than the MHS data and suggest a lower ATMS RMS than MHS. In keeping with Figure 5, an overwhelming amount of data concentrates in the light snowfall region ($\leq$0.5 mm/h) for both ATMS and MHS. In addition, there is an imbalance in the distribution of the data with more data points fall above the 1:1 line than below. This indicates that both ATMS SFR and MHS SFR have an underestimation issue.

The validation statistics in Table 4 quantify the above analyses, i.e., ATMS has a higher correlation coefficient (0.52) than MHS (0.47) and a lower RMS (0.55 mm/h) than MHS (0.69 mm/h), and both have negative bias at $-$0.07 mm/h and $-$0.1 mm/h, respectively. The statistics are generally comparable to the calibration statistics for both instruments but with slightly larger bias and smaller RMS. The underestimation (negative bias) is likely caused by not taking into account the effect of supercooled cloud liquid water in the RTM. Contrary to the cooling effect of ice scattering on T_b, cloud liquid water can elevate T_b through emission hence masking the scattering signal from snowfall [*Liu and Seo*, 2013]. *Wang et al.* [2013] estimated that about 72% of snowing clouds contain supercooled cloud liquid water.

SFR performance for the historical 2016 U.S. East Coast Blizzard [*Robinson*, 2016; *Greybush et al*., 2017] was analyzed and is presented here as a validation case study. The intense nor'easter hit the Mid-Atlantic Region on 22–24 January 2016 and produced record snowfall in many local areas. The SFR product successfully captured the evolution of the snowstorm with snowfall rate estimates from the five satellites. Figure 7 shows a sequence of SFR images in an Advanced Weather Interactive Processing System (AWIPS)-like display and the images of the corresponding MRMS instantaneous snowfall estimates. The snowfall patterns from

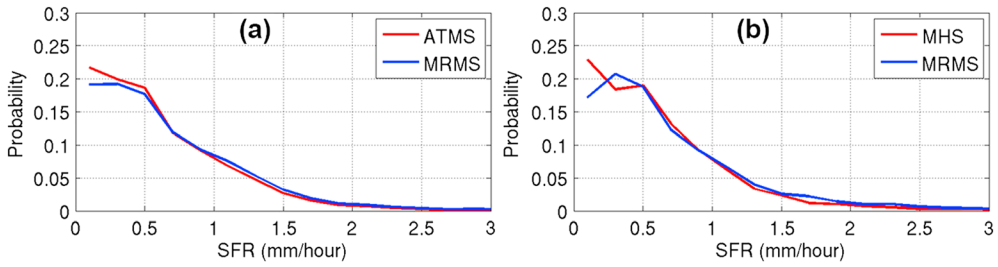

Figure 5. Validation: comparison of PDFs between (a) ATMS SFR and MRMS instantaneous snowfall rate and (b) MHS SFR and MRMS instantaneous snowfall rate.

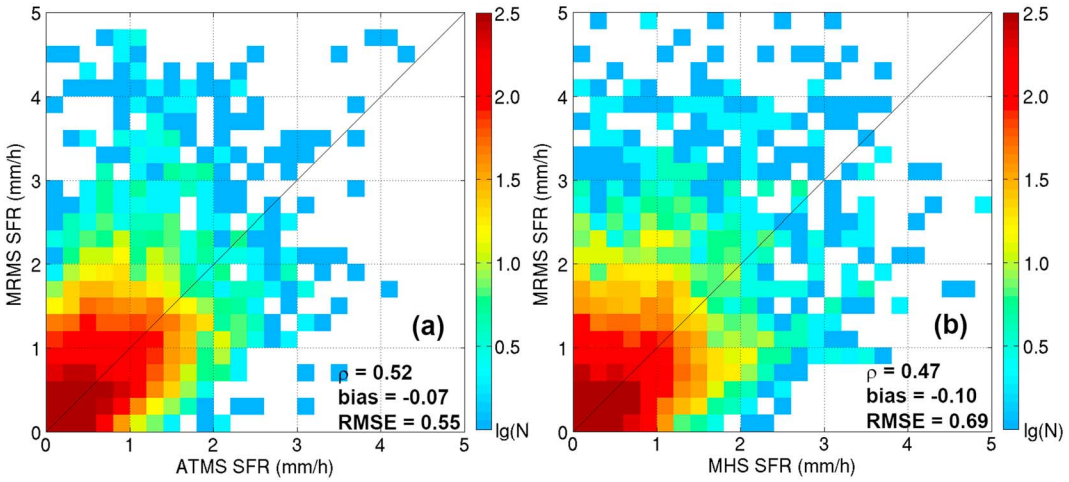

Figure 6. Validation: (a) MRMS snowfall rate versus ATMS SFR scatterplot and (b) MRMS snowfall rate versus MHS SFR scatterplot. Colors represent data density.

the SFR product generally resemble those of the MRMS snowfall data. The SFR statistics from this case (Table 5) demonstrate once again that ATMS SFR outperforms its MHS counterpart with a correlation coefficient of 0.6 for ATMS and 0.54 for MHS and much lower bias. It is noted that both the statistics in Table 5 and the images in Figure 7 are based on ATMS SFR collocated with MRMS data that have 30 min time shift.

The SFR retrievals are also compared to climatology of gauge snowfall observations. Figure 8a presents the January average total snowfall computed from ATMS SFR over the CONUS from 2015 to 2016, and Figure 8b shows the gauge January average total snowfall from 1981 to 2010 [*Durre et al.*, 2013]. The total snowfall is in solid form. A standard 10:1 snow to liquid ratio was assumed to convert ATMS SFR to solid snowfall. While the images in Figure 8 are not from the same time period and large uncertainty may exist in the assumption about snow to liquid ratio, the total snowfall reflects snowfall tendency in CONUS which generally conforms to climatic norm when averaged over a period of time. Therefore, snowfall patterns shown in these images are more revealing than the absolute snow amount. The heavy snowfall along the Rockies and in the northeast has very similar patterns in the ATMS SFR and the gauge snowfall images. Snow in the Great Plains and the Midwest is also mostly comparable between the satellite product and the gauge observations. There are some notable differences in the two images, particularly in the "snowbelt" in the Great Lakes region and along a few mountain ranges: the Cascades in Oregon, the Sierra Nevada in California, and the Appalachians in West Virginia. The snowfall in the snowbelt is overwhelmingly lake effect snow, while the dominant mechanism to generate snowfall in these mountain ranges is orographic forcing. Lake effect snow is characterized by narrow bands of often intense snowfall that occurs when cold air passing over warm water of large lakes. It is associated with shallow convective processes and has abundant supercooled liquid water in the clouds. PMW observations generally are not very sensitive to hydrometeors in such shallow clouds. The emission effect of liquid water further diminishes the scattering signal from ice particles. In addition, the snow bands of lake effect snow usually have widths finer than satellite FOV hence does not carry enough weight when averaged over the entire FOV. Consequently, the SFR algorithm has difficulty detecting lake effect snow or, when the snowfall is detected, it underestimates the intensity. Orographic precipitation is caused by a large-scale air mass moving upward on the windward side of a mountain. The moisture in the air condenses as it ascends and eventually falls back down as precipitation. Orographic snowfall is another example of a shallow snowfall system that may contain copious supercooled cloud liquid water [*Kusunoki et al.*, 2004]. The Cascades and Sierra Nevada Mountains block the westerly wind that carries moisture from the Pacific Ocean and often create intense orographic snowfall in the winter season [*Meyers et al.*, 2011]. While the Appalachian Mountains are not adjacent to any large lakes, its orographic snowfall is often

Table 4. Validation Statistics of the SFR Algorithm

	Correlation Coefficient	Bias (mm/h)	RMS (mm/h)
ATMS	0.52	−0.07	0.55
MHS	0.47	−0.10	0.69

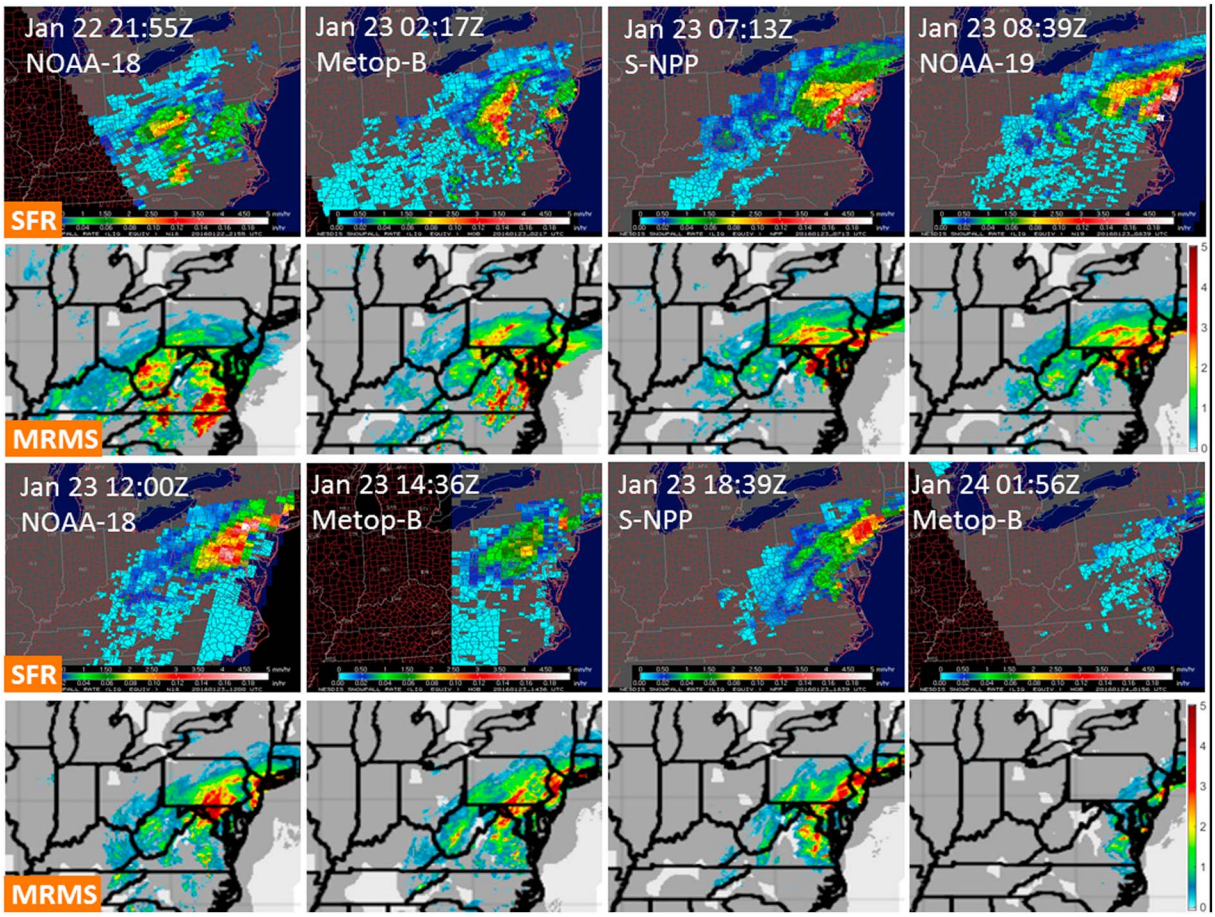

Figure 7. (first and third rows) SFR in AWIPS format and the (second and fourth rows) MRMS instantaneous snowfall rate estimates with 30 min shift during the East Coast Blizzard on 22–24 January 2016.

enhanced by moisture carried to the mountain range by strong wind flowing off the Great Lakes [*Abraham*, 2014]. In much the same way that the current SFR algorithm is not suitable for lake effect snow, it also underperforms for the shallow orographic snowfall that contains abundant liquid water. Effort is underway to incorporate the emission effect of liquid water in the SFR algorithm. It is expected that the new development will lead to improved algorithm performance for some orographic snowfall. It remains to be seen if the enhanced algorithm is applicable to lake effect snow which is more challenging than orographic snowfall because of its narrow snow bands.

4.2. Error Analysis

The SFR algorithm includes some assumptions that can cause various degrees of uncertainty in the retrievals. Some major assumptions are examined in this section for their impact on the SFR product. These include the uncertainty that is unique to the SFR algorithm and those similar to what *Yan et al.* [2008] studied in the context of emissivity retrieval since both algorithms employ the same 1DVAR approach.

4.2.1. Effect of Ice Particle Mass Density

In the SFR algorithm, the mass density of ice particle is assumed to be 600 kg/m^3, i.e., a constant. Two sets of experiments were conducted to quantify the effect of ice density on SFR: (i) the mass density was systematically changed and was applied only to the RTM, while it remains at 600 kg/m^3 for the rest of the SFR algorithm and (ii) the densities were applied to the entire algorithm. Data used in this study were ATMS

Table 5. SFR Statistics From the 2016 U.S. East Coast Blizzard

	Correlation Coefficient	Bias (mm/h)	RMS (mm/h)
ATMS	0.60	−0.14	0.79
MHS	0.54	−0.53	0.88

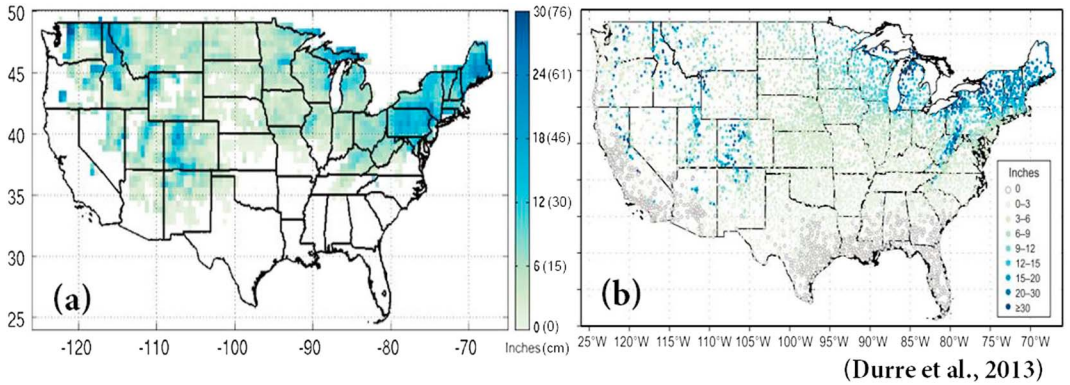

Figure 8. (a) ATMS SFR January average total snowfall from 2015 to 2016 and (b) Gauge January average total snowfall from 1981 to 2010 [*Durre et al.*, 2013].

measurements from 10 days in February and March of 2015 and January and February of 2016. The data were over CONUS because there was snowfall over large area of CONUS on those days. There were more than 100,000 snowfall data points in the data set. Unless otherwise noted, all analyses in this section were performed using this data set. Since the MHS and ATMS SFR algorithms follow the same approach, the conclusions from the error analyses described here are expected to be mostly applicable to the MHS algorithm even though there are some differences between the two such as the frequencies.

Figure 9 shows the mean and standard deviation (as error bar) of the difference in SFR (ΔSFR) between using the various mass densities and using density of 600 kg/m^3 in the RTM. ΔSFR increases with both SFR (density = 600 kg/m^3) and with the density difference, Δd. Smaller mass density results in larger SFR if the density change is limited to the RTM. The change is less than about 7% if Δd is 50 kg/m^3 and less than about 12% if Δd is 100 kg/m^3. The only exception (and the maximum) ΔSFR is 14% with mass density equals to 500 kg/m^3 and SFR (density = 600 kg/m^3) is between 4 and 5 mm/h.

Besides its effect on scattering properties, the mass density of ice particle also impacts its fall velocity (equation (1)). This impact appears to counter the effect of the scattering property change caused by changing mass density (equation (10)). Table 6 gives the mean ΔSFR between using various mass densities and using mass density of 600 kg/m^3 if the same mass density is applied to the entire SFR algorithm. The maximum ΔSFR-to-mean-SFR ratio is −1.6% if mass density is 500 kg/m^3 and SFR is less than 1 mm/h. The maximum absolute mean ΔSFR is 0.06 mm/h or 1.25% if mass density is 500 kg/m^3 and SFR is between 4

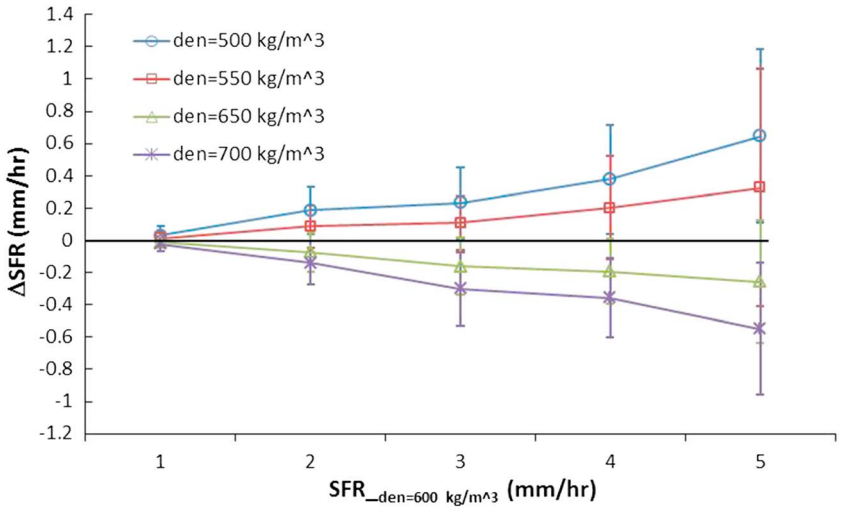

Figure 9. Mean and standard deviation (as error bar) of SFR difference (ΔSFR) between using various mass densities and using mass density equaling to 600 kg/m^3 in the RTM.

and 5 mm/h. While the impact of mass density on RTM retrieval (hence on SFR) is noticeable, the above analysis shows that the effect is largely canceled by the opposite effect of mass density exerted on ice particle fall velocity. It is concluded that at least for the snowfall cases examined, the assumption about fixed mass density of 600 kg/m^3 has a small impact on the overall SFR retrievals.

4.2.2. Effect of Ice Particle Size Distribution

From *Yan et al.* [2008], the assumptions about ice particle size distribution can have a considerable impact on simulated T_bs if I_w and D_e are large, a condition usually corresponds to intense snowfall in cold season. For instance, if the shape parameter for ice particle distribution, ν, increases from 1 (used in the RTM) to 1.5, it can result in an increase of 3.3 K and 8.9 K, respectively, in T_bs at 89 and 150 GHz when both I_w and D_e are 0.2 mm [*Yan et al*., 2008]. Given the magnitude of the impact ν has on T_bs, a sensitivity study on SFR to T_bs was carried out to examine the effect of ice particle size distribution on SFR.

The ATMS SFR is retrieved using measurements at 23.8, 31.4, 88.2, 165.5, and 183.31 ± 7 GHz. These frequencies have varying degree of importance and respond differently to the retrievals. A study using the data set described in section 4.2.1 shows that the correlation coefficients between the retrieved SFR and the above frequencies are, respectively, 0.09, 0.10, 0.11, 0.53, and 0.70. The statistics reveal that 165.5 GHz and 183.31 ± 7 GHz have much larger impact on SFR than the other three channels. Therefore, the following analysis will focus on these two frequencies. Further regression study on the data set (figure not included) shows that for every 1 mm/h increase in SFR, T_b at 165.5 GHz decreases by about 10 K and T_b at 183.31 ± 7 GHz by about 6.5 K. This T_b ratio between the two frequencies will be used in analysis below except in some special cases. Figure 10a displays the mean and standard deviation of ΔSFR when T_b at 165.5 GHz is perturbed by up to ±10 K and 183.31 ± 7 GHz by up to ±6.5 K. Figure 10b shows the mean ΔSFR to mean SFR ratios (as percentages) for the same T_b perturbations. From the figures, negatively perturbed T_bs represent increased scattering from ice particles hence increased SFR. The larger the magnitude of the negative perturbation, the more intense the snowfall. Positively perturbed T_bs weaken snowfall by various degrees depending on the magnitude of the perturbation. All ΔSFR are around or less than 0.4 mm/h except when perturbations at 165.5 GHz and 183.31 ± 7 GHz are −10 K and −6.5 K, respectively. In the latter case, the mean Δ(SFR) changes from 0.34 mm/h to 0.88 mm/h for mean SFR ranging from 0 mm/h to around 5 mm/h. Figure 10b shows that light snow has the largest percentage changes as a result of the perturbation. At the high end of SFR, the maximum change is about 10% with positive perturbation and about 20% with negative perturbation. Mean SFR changes by 20% to almost 70% for heavy to light snowfall if 165.5 GHz and 183.31 ± 7 GHz are perturbed by −10 K and −6.5 K, respectively. Based on *Yan et al.* [2008], T_bs under heavy snowfall can change on orders similar to such perturbation if ν deviates significantly from 1. The above analysis reveals the importance of ice particle size distribution to the accuracy of SFR retrieval especially for intense snowfall. This is an area that will be further studied in the future.

4.2.3. Effect of Ice Particle Shape

Natural snow particles can have shapes of various pristine habits or form aggregates. The SFR algorithm was developed based on the assumption of spherical ice habit. To examine the effect of this simplistic assumption, the scattering properties of spherical habit and three nonspherical ice habits from *Liu* [2004] were used in the 1DVAR to retrieve SFR. The three nonspherical shapes were rosettes, sector (type-A snowflake), and dendrite (type-B snowflake). MHS measurements from five snowfall events in February 2014 and January and February of 2015 were used in this study. Close to 10,000 MHS SFR retrievals were collocated with MRMS snowfall data, and their scatterplots are presented in Figure 11 along with the linear regression lines and the corresponding statistics. While the spherical shape habit results in the highest correlation with the radar estimates ($r = 0.58$) among the four shapes examined, the minimum RMS is achieved with the rosettes. Dendrites appear to have the worst overall statistics with much larger RMS and bias than the other ice particle shapes. It is noted that some studies have found that sectors gave the best simulation results among the four shapes [e.g., *Geer and Baordo*, 2014]. The statistics in Figure 11 demonstrate that the assumption of spherical particle shape leads to reasonable algorithm performance.

Aggregates are a common occurrence and prevail when temperature is between 0°C and −5°C [*Hobbs et al*., 1974]. *Kuo et al.* [2016] built a large database of the scattering properties of pristine ice habits and snow aggregates. Figures 12a and 12b are from *Kuo et al.* [2016] and show the extinction efficiency and asymmetry parameter versus liquid-equivalent snow particle diameter for 165.5 GHz frequency. Included in the figures are the scattering properties of a vast number of nonspherical habits and aggregates as well as those of

Table 6. Mean ΔSFR*-to-SFR Ratio (%)[a]

SFR (mm/h) Range	0–1	1–2	2–3	3–4	4–5
Den = 500 kg/m^3	−1.63	0.76	−0.37	−0.54	1.25
Den = 550 kg/m^3	−0.82	0.07	−0.36	−0.26	0.30
Den = 650 kg/m^3	0.66	0.29	−0.54	−0.78	0.10
Den = 700 kg/m^3	0.69	0.88	−0.85	−0.86	−0.05

[a]The same mass density is applied to the entire SFR algorithm.

spherical habits with various densities calculated using Mie code. The spherical habit densities shown in Figure 12 are size dependent [*Heymsfield et al*., 2010], 0.1 g/cm^3, and 0.3 g/cm^3. Recall that the density of spherical ice particle is assumed to be 0.6 g/cm^3 in the SFR algorithm. The extinction efficiency of spherical habit is closest to that of the nonspherical habits and aggregates when the constant density is 0.3 g/cm^3. The same conclusion can be drawn for the asymmetry parameter. Note that the range of the liquid-equivalent snow particle diameter in Figure 12 is more suitable for aggregates than for pristine habit. In the SFR computation, D_e is generally less than 0.5 mm. Figure 12 shows that the scattering properties of the spherical and nonspherical/aggregate particles agree well with each other in this size range. It would be desirable to adopt more realistic ice particle shapes in simulating T_bs in the 1DVAR. However, it is a challenging quest to determine the appropriate particle shapes to use for each snowstorm given the lack of information on cloud microphysics. A potential solution might be to use a mixture of retrievals from different ice habits and aggregates.

4.2.4. Effect of Two-Stream, One-Layer RTM

The RTM used in the 1DVAR for forward simulation is a two-stream, one-layer model [*Yan et al*., 2008]. While bias correction is performed within the model, it is expected that there will be residual errors in the simulated T_bs. In fact, the convergence thresholds for the differences between simulated and observed T_bs are a manifestation of the uncertainty. Some analysis was performed to investigate the effect of employing the two-stream, one-layer RTM on SFR retrievals. Figure 13 presents the nonconvergence rate for given convergence thresholds at the five frequencies used in the RTM. The black circle marks the nonconvergence rate (~10%) of the SFR algorithm based on the data set used, i.e., 90% of all detected snowfall is retrieved with 3 K or less bias at 183 ± 7 GHz and 1.5 K or less at other channels. From Figure 10a, T_b bias at this level will cause −0.01 to 0.38 mm/h bias in SFR under light to intense snowfall. The nonconvergence rate decreases quickly with T_b convergence thresholds and plateaus as the thresholds become large. For thresholds of 4 K for 183 ± 7 GHz and 3 K for other frequencies, the nonconvergence rate is about 4%. With these thresholds, SFR bias ranges from about 0.1 mm/h to about 0.5 mm/h for light to intense snowfall (Figure 10a). To be consistent with Figure 10a, the unlikely thresholds of 6.5 K and 10 K were applied to 183 ± 7 GHz and other frequencies, respectively. Figure 13 shows that it results in a nonconvergence rate less than 0.5% and adds 0.34 mm/h to 0.88 mm/h bias to SFR retrievals depending on snowfall intensity. These results demonstrate that the two-stream, one-layer RTM performs reasonably well at simulating T_bs at the five frequencies for the snowfall data examined, and the residual T_b bias only lead to limited SFR bias.

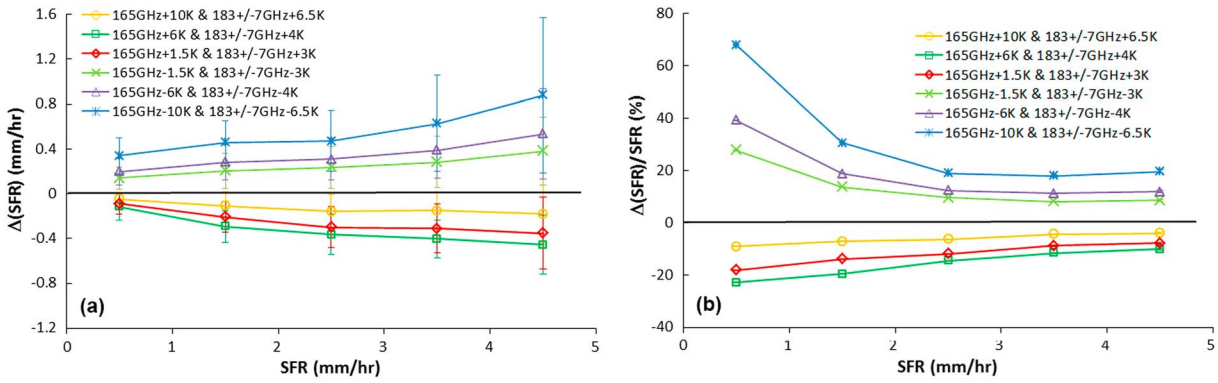

Figure 10. ΔSFR from T_b perturbation at 165.5 GHz and 183.31 ± 7 GHz, (a) as absolution change and (b) as percentage change. The perturbation values are given in the plots.

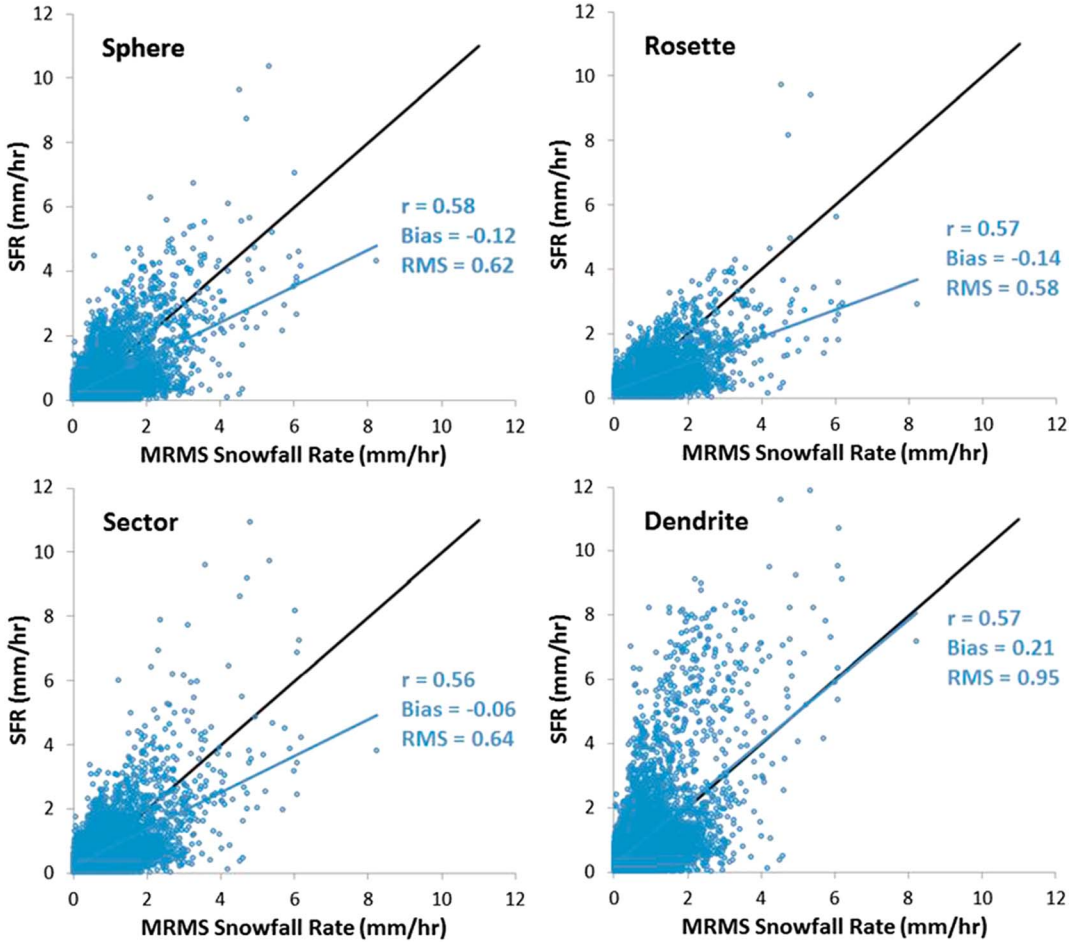

Figure 11. SFR retrievals versus collocated MRMS snowfall rate for four different ice habits: sphere, rosette, sector, and dendrite.

4.2.5. Assumption About IWC Distribution

Since IWC profile is not known from the passive microwave measurements or the GFS model, IWC is initially assumed to be uniformly distributed in cloud column to simplify the development of the SFR equation (equation (10)). This assumption clearly underestimates SFR since IWC generally increases from the upper portion to the lower portion of clouds. Therefore, the SFR algorithm is so designed that a bulk adjustment is applied to equation (10) to compensate for the nonuniform IWC distribution (equations (11)–(13)). The adjustment was derived from two sets of radar precipitation data: Stage IV (including gauge data) and MRMS (section 3.2). It is noted that the adjustment for IWC is not limited to utilizing radar derived snowfall rate data. However, the radar product, especially MRMS, is the optimal data to calibrate (and validate) SFR. The adjustment derived from Stage IV is a constant which modifies the initial satellite retrievals linearly (Figure 14). The adjustment from MRMS is a nonlinear function (equations (14) and (15)) and leads to nonlinear adjustment of the initial satellite retrievals (Figure 14). In terms of IWC distribution, the linear adjustment is equivalent to a constant ratio between the average IWC and the effective IWC, IWC_e (section 3.2). In contrast, the average IWC to IWC_e ratio is a function of the initial SFR in the case of nonlinear adjustment. The latter outperforms the linear adjustment possibly because it better captures the distribution of IWC.

Table 7 lists the performance statistics of SFR before and after each adjustment. It is important to point out that the adjustment, either linear or nonlinear, is an intrinsic part of the SFR algorithm to compensate for the nonuniform distribution of IWC. The adjustment reduces the retrieval bias and RMS but has little impact on the general structure of the retrieved SFR field within a snowstorm, which can be measured by

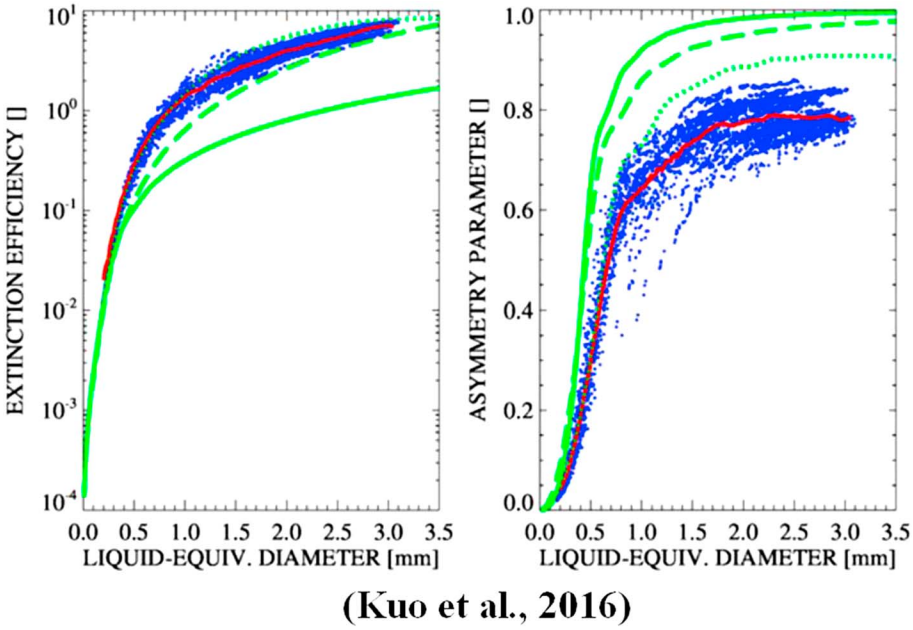

Figure 12. Scattering properties of various ice particles as function of liquid-equivalent particle diameter at 165.5 GHz [from *Kuo et al*., 2016].

the correlation between SFR and MRMS precipitation data (used as "truth"). This statement is supported by the constant correlation coefficient before and after adjustments given in Table 7. It demonstrates that the correlation between SFR and MRMS is achieved from the 1DVAR-based algorithm rather than from the adjustment for IWC. Table 7 shows that the adjustment significantly reduces the bias and RMS introduced by the assumption about IWC distribution. The residual bias and RMS are a combination of uncertainties caused by other assumptions made in the algorithm and individual IWC adjustment deviates from the bulk adjustment. As mentioned above, the information on individual IWC profile is not available from satellite or model especially in near real time.

4.2.6. Uncertainty From NPW Model

GFS model data are used in the SFR algorithm to derive cloud properties and ice particle fall velocity. This means that some model uncertainty can propagate to the SFR algorithm. However, analyses indicate that model bias does not cause significant error in the rate retrieval. For instance, a 10% increase in TPW only results in 2.6% to 1.3% increase in SFR that ranges from 0 to 5 mm/h. For the same range of SFR, adding 1°C to the surface temperature leads to 1.3% to 0.1% change in SFR. GFS surface pressure and 2 m temperature and water vapor are used to derive air density and dynamic viscosity. Model errors in these variables cause little change in the air properties hence minor influence on SFR retrievals.

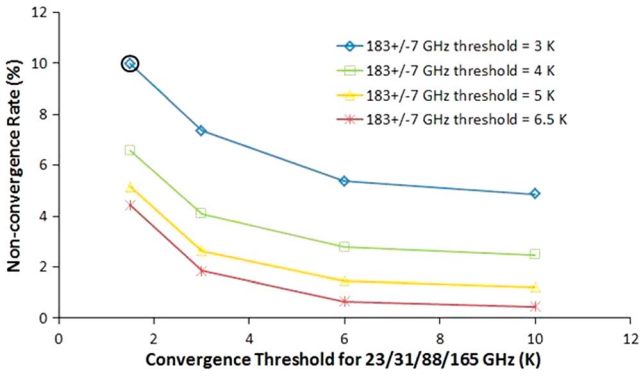

Figure 13. The 1DVAR nonconvergence rate as a function of T_b convergence thresholds for 23.8, 31.4, 88.2, 165.5, and 183 ± 7 GHz.

The error analyses in this section show that the SFR algorithm includes various uncertainty sources such as the significant impact of ice particle size distribution, moderate influence from the assumption about ice particle shape, and the minor effect from ice particle density and model errors. Snowfall is the result of highly complex and dynamic processes under the influences of both the atmosphere and the surface. Many of the

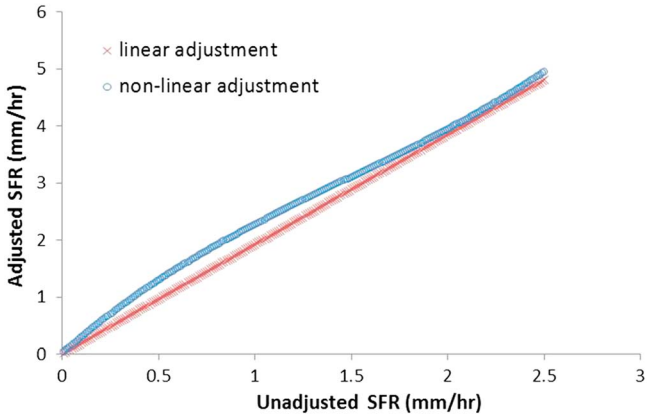

Figure 14. SFR after IWC-based adjustments versus before adjustments.

parameters involved in the physical framework are not readily available and have to rely on optimal and yet feasible assumptions or be estimated through statistical means. The validation study described in section 4.1 is an overall evaluation of the algorithm with all its uncertainties caused by the various assumptions and approximations. The validation statistics in Table 4 show that the SFR estimates have high correlation (for passive microwave snowfall rate product) with radar snowfall rate, low bias, and reasonable RMS.

5. Summary and Conclusions

A physically based, overland SFR algorithm has been developed for PMW radiometers AMSU-A/MHS pair aboard the NOAA POES and EUMETSAT Metop satellites, and ATMS aboard the Suomi-NPP and future JPSS satellites. The algorithm relies on a separate SD model [*Kongoli et al*., 2015] to detect snowfall. The SD model is further enhanced with a set of NWP model-based filters. These filters, especially the cloud thickness threshold, are very effective at removing false alarms in the SD model. The SFR algorithm is composed of four main elements: cloud properties retrieval, computation of ice particle terminal velocity, IWC adjustment, and the determination of snowfall rate. Cloud properties, I_w and D_e, are retrieved using a 1DVAR approach [*Yan et al*., 2008] that uses a two-stream, one-layer RTM [*Weng et al*., 2001; *Yan et al*., 2008] as forward model to simulate T_bs at several window and water vapor sounding channels. The model developed by *Heymsfield and Westbrook* [2010] is adopted to calculate ice particle terminal velocity. The retrieved cloud properties are used in the computation of the terminal velocity and IWC. The IWC is further modified with an adjusting function that was derived from histogram matching SFR with radar precipitation data. Finally, SFR is determined from the modified IWC and ice particle terminal velocity. When the above steps are combined into a single mathematical expression, SFR becomes a function of a complex integral (equation (10)) which can only be solved numerically. This is realized using Romberg's method.

The SFR product has been validated using both MRMS radar precipitation data [*Zhang et al*., 2016] and gauge observations [*Durre et al*., 2013]. Three types of validation studies are presented: statistical analysis of collocated satellite and radar instantaneous snowfall data from a collection of snowfall events, case study, and comparison of SFR and gauge snowfall climatology. The results show that the SFR product and the radar snowfall data correlate well with correlation coefficients above 0.5. In the case of the 2016 East Coast Blizzard, the correlation coefficient between ATMS SFR and MRMS reaches 0.6. The study also reveals that SFR has a dry bias compared to radar. This is likely caused by not taking into consideration the emission effect of supercooled liquid water in the RTM. The climatology comparison shows that SFR has similar snow patterns as gauge observations in most parts of CONUS except where shallow snowfall dominates especially when it is accompanied with abundant supercooled cloud liquid water. This includes the snowbelt in the Great Lakes region where lake effect snow dominates and some mountain ranges where shallow orographic

Table 7. SFR Performance Statistics Against MRMS Before and After Each IWC Adjustment

	ATMS			MHS		
	Correlation Coefficient	Bias (mm/h)	RMS (mm/h)	Correlation Coefficient	Bias (mm/h)	RMS (mm/h)
Before adjustment	0.55	−0.82	1.07	0.47	−0.76	0.99
After linear adjustment	0.55	−0.30	0.77	0.47	−0.33	0.75
After nonlinear adjustment	0.55	−0.03	0.67	0.47	−0.03	0.74

snowfall prevails. A major task being planned is to incorporate the effect of supercooled cloud liquid water in the SFR algorithm. This will be accomplished by modifying the RTM and including cloud liquid water in the control vector. The current version of the RTM only accounts for the effect of cloud ice. Including liquid water effect in the RTM is expected to improve the performance of the SFR algorithm in the future. Finally, a set of error analyses were carried out to examine the uncertainties introduced by the various assumptions made in the SFR algorithm. The analyses revealed that the uncertainty sources range from significant impact from ice particle size distribution, moderate influence from ice particle shape, and minor effect from ice particle density and NWP model errors, etc.

Acknowledgments

The authors would like to thank Brad Ferrier, Ruiyu Sun, and Shrinivas Moorthi for answering the authors' questions about the GFS data, Jian Zhang for helping with the MRMS data, and Brian Carcione for providing information on precipitation classification utilized at NWS. The support from the JPSS Proving Ground and Risk Reduction was crucial to the development of the more advanced SFR algorithm. This research has been supported by NOAA and the JPSS Program through grant NA09NES4400006 (Cooperative Institute for Climate and Satellites-CICS) at the University of Maryland, Earth System Science Interdisciplinary Center (ESSIC). The views, opinions, and findings contained in this report are those of the authors and should not be construed as an official National Oceanic and Atmospheric Administration or U.S. Government position, policy, or decision. The AMSU-A, MHS, ATMS satellite data and the SFR product data can be obtained from NOAA Comprehensive Large Array-data Stewardship System (CLASS) (www.class.noaa.gov). The MRMS radar precipitation data are available at http://mrms.ncep.noaa.gov/data/. The GFS model data are downloadable from NOAA National Operational Model Archive and Distribution System (NOMADS) (https://www.ncdc.noaa.gov/data-access/model-data/model-datasets/global-forcast-system-gfs).

References

Abraham, L. (2014), The Shenandoah Valley, An Orographic Hotspot. [Available at http://www.theweatherprediction.com/weatherpapers/001/index.html.]

Aires, F., C. Prigent, F. Bernardo, C. Jiménez, R. Saunders, and P. Brunel (2011), A Tool to Estimate Land-Surface Emissivities at Microwave frequencies (TELSEM) for use in numerical weather prediction, *Q. J. R. Meteorol. Soc.*, *137*(656), 690–699, doi:10.1002/qj.803.

Bauer, P., and R. Bennartz (1998), Tropical rainfall measuring mission microwave imaging capabilities for the observation of rain clouds, *Radio Sci.*, *33*, 335–349, doi:10.1029/97RS02049.

Bennartz, R., and P. Bauer (2003), Sensitivity of microwave radiances at 85–183 GHz to precipitating ice particles, *Radio Sci.*, *38*(4), 8075, doi:10.1029/2002RS002626.

Durre, I., M. F. Squires, R. S. Vose, X. Yin, A. Arguez, and S. Applequist (2013), NOAA's 1981–2010 U.S. climate normals: Monthly precipitation, snowfall, and snow depth, *J. Appl. Meteorol. Climatol.*, *52*, 2377, doi:10.1175/JAMC-D-13-051.1.

Evans, K. F., J. Turk, T. Wong, and G. L. Stephens (1995), A Bayesian approach to microwave precipitation profile retrieval, *J. Appl. Meteorol.*, *34*(1), 260–279, doi:10.1175/1520-0450-34.1.260.

Ferraro, R. R., and G. F. Marks (1995), The development of SSM/I rain-rate retrieval algorithms using ground-based radar measurements, *J. Atmos. Ocean. Technol.*, *12*(4), 755–770, doi:10.1175/1520-0426(1995)012<0755:TDOSRR>2.0.CO;2.

Ferraro, R. R., F. Weng, N. C. Grody, L. Zhao, H. Meng, C. Kongoli, P. Pellegrino, S. Qiu, and C. Dean (2005), NOAA operational hydrological products derived from the Advanced Microwave Sounding Unit, *IEEE Trans. Geosci. Remote Sens.*, *43*, 1036–1049, doi:10.1109/TGRS.2004.843249.

Foster, J. L., G. Skofronick-Jackson, H. Meng, J. R. Wang, G. Riggs, P. J. Kocin, B. T. Johnson, J. Cohen, D. K. Hall, and S. V. Nghiem (2012), Passive microwave remote sensing of the historic February 2010 snowstorms in the Middle Atlantic Region of the USA, *Hydrol. Process.*, *26*(22), 3459–3471, doi:10.1002/hyp.8418.

Geer, A., and F. Baordo (2014), Improved scattering radiative transfer for frozen hydrometeors at microwave frequencies, *Atmos. Meas. Tech.*, *7*, 1839–1860, doi:10.5194/amt-7-1839-2014.

Greybush, S. J., S. Saslo, and R. Grumm (2017), Assessing the ensemble predictability of precipitation forecasts for the January 2015 and 2016 East Coast winter storms, *Weather Forecasting*, *32*, doi:10.1175/WAF-D-16-0153.1.

Heymsfield, A. J., and C. D. Westbrook (2010), Advances in the estimation of ice particle fall speeds using laboratory and field measurements, *J. Atmos. Sci.*, *67*(8), 2469–2482, doi:10.1175/2010JAS3379.1.

Heymsfield, A. J., C. Schmitt, A. Bansemer, and C. H. Twohy (2010), Improved representation of ice particle masses based on observations in natural clouds, *J. Atmos. Sci.*, *67*(10), 3303–3318, doi:10.1175/2010JAS3507.1.

Hobbs, P., S. Chang, and J. D. Locatelli (1974), The dimensions and aggregation of ice crystals in natural clouds, *J. Geophys. Res.*, *79*, 2199–2206, doi:10.1029/JC079i015p02199.

Kidd, C., T. Matsui, J. Chern, K. Mohr, C. Kummerow, and D. Randel (2016), Precipitation estimates from cross-track passive microwave observations using a physically based retrieval scheme, *J. Hydrometeorol.*, *17*, 383–400, doi:10.1175/JHM-D-15-0051.1.

Kidder, S. Q., and A. S. Jones (2007), A blended satellite total precipitable water product for operational forecasting, *J. Atmos. Ocean. Technol.*, *24*(1), 74–81, doi:10.1175/JTECH1960.1.

Kim, M.-J., J. A. Weinman, W. S. Olson, D.-E. Chang, G. Skofronick-Jackson, and J. R. Wang (2008), A physical model to estimate snowfall over land using AMSU-B observations, *J. Geophys. Res.*, *113*, D09201, doi:10.1029/2007JD008589.

Kongoli, C., P. Pellegrino, R. Ferraro, N. C. Grody, and H. Meng (2003), A new snowfall detection algorithm over land using measurements from the Advanced Microwave Sounding Unit (AMSU), *Geophys. Res. Lett.*, *30*(14), 1756, doi:10.1029/2003GL017177.

Kongoli, C., H. Meng, J. Dong, and R. Ferraro (2015), A snowfall detection algorithm over land utilizing high-frequency passive microwave measurements—Application to ATMS, *J. Geophys. Res. Atmos.*, *120*, 1918–1932, doi:10.1002/2014JD022427.

Kummerow, C. D., S. Ringerud, J. Crook, D. Randel, and W. Berg (2011), An observationally generated a priori database for microwave rainfall retrievals, *J. Atmos. Ocean. Technol.*, *28*(2), 113–130, doi:10.1175/2010JTECHA1468.1.

Kummerow, C., D. Randel, M. Kulie, N.-Y. Wang, R. Ferraro, S. J. Munchak, and V. Petkovic (2015), The evolution of the Goddard Profiling algorithm to a fully parametric scheme, *J. Atmos. Ocean. Technol.*, *32*(12), 2265–2280, doi:10.1175/JTECH-D-15-0039.1.

Kusunoki, K., M. Murakami, M. Hoshimoto, N. Orikasa, Y. Yamada, H. Mizuno, K. Hamazu, and H. Watanabe (2004), The characteristics and evolution of orographic snow clouds under weak cold advection, *Mon. Weather Rev.*, *132*(1), 174–191, doi:10.1175/1520-0493(2004)132<0174:TCAEOO>2.0.CO;2.

Kuo, K.-S., W. S. Olson, B. T. Johnson, M. Grecu, L. Tian, T. L. Clune, B. H. van Aartsen, A. J. Heymsfield, L. Liaos, and R. Meneghini (2016), The microwave radiative properties of falling snow derived from nonspherical ice particle models. Part I: An extensive database of simulated pristine crystals and aggregate particles, and their scattering properties, *J. Appl. Meteorol. Climatol.*, *55*(3), 691–708, doi:10.1175/JAMC-D-15-0130.1.

Lin, Y., and K. E. Mitchell (2005), The NCEP Stage II/IV hourly precipitation analyses: Development and applications, 19th Conf. on Hydrology, Am. Meteorol. Soc., San Diego, Calif., 9-13 Jan., Pap. 1.2.

Liu, G. (2004), Approximation of single scattering properties of ice and snow particles for high microwave frequencies, *J. Atmos. Sci.*, *61*(20), 2441–2456, doi:10.1175/1520-0469(2004)061<2441:AOSSPO>2.0.CO;2.

Liu, G., and E.-K. Seo (2013), Detecting snowfall over land by satellite high-frequency microwave observations: The lack of scattering signature and a statistical approach, *J. Geophys. Res. Atmos.*, *118*, 1376–1387, doi:10.1002/jgrd.50172.

Meyers, M., J. Steenburgh, and D. Wesley (2011), Cool-season orographic precipitation processes and prediction, AWOC Winter Weather Track, IC5.6. [Available at http://www.wdtb.noaa.gov/courses/winterawoc/documents/color_PDFs/IC56.pdf.]

Mitchell, D. L. (1996), Use of mass- and area-dimensional power laws for determining precipitation particle terminal velocities, *J. Atmos. Sci.*, *53*(12), 1710–1723, doi:10.1175/1520-0469(1996)053<1710:UOMAAD>2.0.CO;2.

Noh, Y.-J., G. Liu, E.-K. Seo, J. R. Wang, and K. Aonashi (2006), Development of a snowfall retrieval algorithm at high microwave frequencies, *J. Geophys. Res.*, *111*, D22216, doi:10.1029/2005JD006826.

Rauber, R. M., L. S. Olthoff, M. K. Ramamurthy, and K. E. Kunkel (2001a), Further investigation of a physically based, nondimensional parameter for discriminating between locations of freezing rain and ice pellets, *Weather Forecasting*, *16*, 185–191, doi:10.1175/1520-0434(2001)016<0185:FIOAPB>2.0.CO;2.

Rauber, R. M., L. S. Olthoff, M. K. Ramamurthy, D. Miller, and K. E. Kunkel (2001b), A synoptic weather pattern and sounding-based climatology of freezing precipitation in the United States east of the Rocky Mountains, *J. Appl. Meteorol.*, *40*, 1724–1747, doi:10.1175/1520-0450(2001)040<1724:ASWPAS>2.0.CO;2.

Robinson, D. A. (2016), The 2015–2016 U.S. snow report: A slim year with a few surprises, *Weatherwise*, *69*(6), 21–31, doi:10.1080/00431672.2016.1226635.

Skofronick-Jackson, G., M.-J. Kim, J. A. Weinman, and D. E. Chang (2004), A physical model to determine snowfall over land by microwave radiometry, *IEEE Trans. Geosci. Remote Sens.*, *42*(5), 1047–1058, doi:10.1109/TGRS.2004.825585.

Skofronick-Jackson, G., B. T. Johnson, and S. J. Munchak (2013), Detection thresholds of falling snow from satellite-borne active and passive sensors, *IEEE Trans. Geosci. Remote Sens.*, *51*(7), 4177–4189, doi:10.1109/TGRS.2012.2227763.

Stephens, G. L., et al. (2002), The CloudSat mission and the A-Train: A new dimension of space-based observations of clouds and precipitation, *Bull. Am. Meteorol. Soc.*, *83*(12), 1771–1790, doi:10.1175/BAMS-83-12-1771.

Stewart, R. E., and P. King (1987), Freezing precipitation in winter storms, *Mon. Weather Rev.*, *115*, 1270–1280.

Wang, Y., G. Liu, E.-K. Seo, and Y. Fu (2013), Liquid water in snowing clouds: Implications for satellite remote sensing of snowfall, *Atmos. Res.*, *131*, 60–72, doi:10.1016/j.atmosres.2012.06.008.

Weng, F., and N. Grody (2000), Retrieval of ice cloud parameters using a microwave imaging radiometer, *J. Atmos. Sci.*, *57*(8), 1069–1081, doi:10.1175/1520-0469(2000)057<1069:ROICPU>2.0.CO;2.

Weng, F., B. Yan, and N. Grody (2001), A microwave land emissivity model, *J. Geophys. Res.*, *106*, 20,115–20,123, doi:10.1029/2001JD900019.

Weng, F., L. Zhao, R. Ferraro, G. Poe, X. Li, and N. Grody (2003), Advanced microwave sounding unit cloud and precipitation algorithms, *Radio Sci.*, *38*(4), 8068, doi: 10.1029/2002RS002679.

You, Y., N.-Y. Wang, and R. Ferraro (2015), A prototype precipitation retrieval algorithm over land using passive microwave observations stratified by surface condition and precipitation vertical structure, *J. Geophys. Res. Atmos.*, *120*, 5295–5315, doi:10.1002/2014JD022534.

You, Y., N.-Y. Wang, R. Ferraro, and S. Rudlosky (2017), Quantifying the snowfall detection performance of the GPM microwave imager channels over land, *J. Hydrometeorol.*, *18*, 729–751, doi:10.1175/JHM-D-16-0190.1.

Yan, B., F. Weng, and H. Meng (2008), Retrieval of snow surface microwave emissivity from the advanced microwave sounding unit, *J. Geophys. Res.*, *113*, D19206, doi:10.1029/2007JD009559.

Zhang, J., et al. (2011), National Mosaic and Multi-Sensor QPE (NMQ) system: Description, results, and future plans, *Bull. Am. Meteorol. Soc.*, *92*(10), 1321–1338, doi:10.1175/2011BAMS-D-11-00047.1.

Zhang, J., et al. (2016), Multi-Radar Multi-Sensor (MRMS) Quantitative Precipitation Estimation: Initial operating capabilities, *Bull. Am. Meteorol. Soc.*, *97*(4), doi:10.1175/BAMS-D-14-00174.1.